RESEARCH ARTICLE

Kinematics and optimization of a novel 4-DOF two-limb gripper mechanism

Lin Wang[1,2], Yuefa Fang[1] , Dan Zhang[2] and Yi Yang[3]

[1]Department of Mechanical Engineering, Beijing Jiaotong University, Beijing, China, [2]Department of Mechanical Engineering, Faculty of Engineering, The Hong Kong Polytechnic University, Hong Kong, China, and [3]Beijing Aerospace Institute for Metrology and Measurement Technology, Beijing, China
Corresponding author: Yuefa Fang; E-mail: yffang@bjtu.edu.cn

Abstract
This study presents a novel 4-DOF two-limb gripper mechanism with a simple design that offers high adaptability for different objects. The mechanism integrates a three-finger end effector and employs a 2-DOF driving system in both serial kinematic chains mounted on the base, addressing performance problems caused by moving actuators. First, the architecture of the gripper mechanism is described, and its mobility is verified. Next, the inverse and forward kinematic problems are solved, and the Jacobian matrix is derived to analyze the singularity conditions. The inverse and forward singularity surfaces are plotted. The workspace is investigated using a search method, and two indices, manipulability and dexterity, are studied. The proposed manipulator's parameters are optimized for improved dexterity. The novel gripper mechanism has high potential for grasping different types of parts within a large workspace, making it a valuable addition to the field of robotics.

1. Introduction

Parallel manipulators are commonly used in industrial applications due to the merit of high stiffness, carrying capacity, precision, and low movement inertia [1]. Lower-mobility manipulators have attracted extensive attention from scholars because of their simpler structures, lower manufacturing cost, and larger workspaces when compared to 6-DOF manipulators [2–4]. Among lower-mobility manipulators, SCARA motion parallel manipulators, which include three translations in space plus one rotation around a given axis, are preferred for tasks such as material handling, surface mounting, parts assembly, and pick-and-place [5–7].

The Delta robot is the most well-known manipulator that outputs three translations [8], and numerous Delta-based SCARA motion manipulators have been proposed. The common structural feature of these Delta-based manipulators is that four identical limbs connect the base and the rigid moving platform, such as H4 [9], I4 [10], and Par4 [11]. Xie [12] introduced a high-speed parallel robot with Schönflies motion and analyzed kinematic issues. Salgado synthesized a novel 3T1R (T denotes translation and R denotes rotation) fully parallel manipulator using only lower kinematic pairs in ref. [13]. Apart from Delta-based manipulators, many novel SCARA motion manipulators have been designed with different kinematic performances. Tian [14] designed a generalized parallel mechanism for 3T1R motion with the characteristics of partially decoupling motion. Zhao [15] investigated a 3T1R manipulator and optimized its workspace. Alvarado [16] presented the kinematics and dynamics analysis of a 4-PRUR (P is prismatic joint, R is rotational joint, and U is universal joint) parallel manipulator using screw theory and the principle of virtual work. Other novel architectures have been proposed for SCARA motion in the literature [17–20].

The manipulators with simple structures mainly offer the advantages of low manufacturing cost and large workspace. Some two-limb architectures have been presented in the literature [21–25]. However, only one actuated joint in each limb is fixed to the base, which causes an increase in moving mass when the manipulator moves. It is well known that all actuators should be mounted on the base for better dynamic performance.

Human-like hands [26–35] have the ability to perform dexterous manipulations, but they require complex and sophisticated drive systems and sensors, which can lead to high cost and difficulty in design and control. Suction gripping devices [36–38] have been developed for grasping objects in cluttered and narrow spaces, but they can be unstable at high speeds, accelerations, or payloads due to their soft material and variable contact area. Several grasping mechanisms based on parallel mechanisms have been proposed that offer high stiffness, accuracy, and load/weight ratio. Jin [39] designed a novel dexterous hand using three parallel mechanisms as fingers, while Tian [40] synthesized a redundant reconfigurable generalized parallel mechanism capable of grasping objects, and Wang [41] proposed a generalized parallel mechanism with a configurable moving platform suitable for grasping larger or heavier objects. However, these parallel mechanism-based grasping mechanisms have complex structures, which can make control difficult.
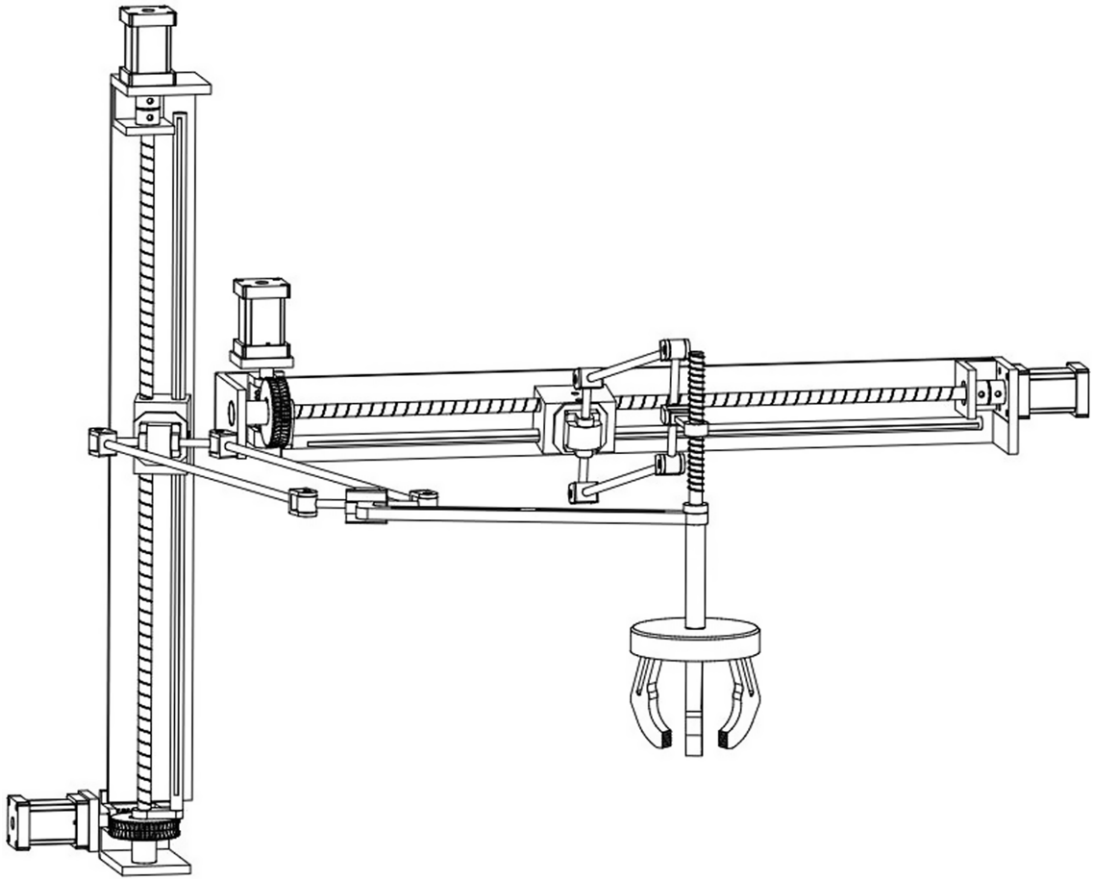
Based on previous studies and tests, it has been identified that the simplicity of the architecture is crucial for effective manipulator design. Therefore, in this paper, we propose a novel two-limb architecture with a small number of lower kinematic pairs to address these requirements. Our approach involves constructing a gripper mechanism based on a two-limb 3T1R mechanism with an integrated three-finger end effector. According to our previous work in ref. [42], a 2-DOF driving system is used, and all actuators are mounted on the base to avoid the issue of a large moving mass caused by moving actuators. In Section 2, we use screw theory to verify the DOF characteristics of the proposed manipulator. In Section 3, we solve the inverse and forward kinematic issues. Subsequently, in Section 4, we evaluate the performance of the proposed manipulator in terms of its workspace, singularity, manipulability, and dexterity. We optimize the parameters of the proposed manipulator for improved dexterity in Section 5. Finally, we draw a conclusion in Section 6.

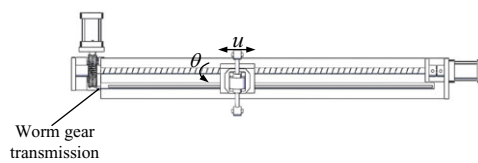## 2. Description and mobility of the gripper mechanism

The proposed novel two-limb gripper mechanism is depicted in Fig. 1, consisting of two serial kinematic chains that connect the base and the end effector. The 2-DOF driving system is employed in both serial kinematic chains to achieve a compact design, as is shown in Fig. 2. The 2-DOF driving system is a PR-drive system, where the prismatic joint and the revolute joint are parallel to each other. The input rotation around the axis perpendicular to the u-direction is transformed by a worm gear drive system to a rotation around the u-direction. The translational direction and rotational angle of the output link are denoted by u and θ, respectively, and are controlled by two actuators. A revolute joint is used to connect the two serial kinematic chains, and the three-finger device is mounted on the revolute joint. By rotating the screw, the opening and closing of the three-finger end effector can be achieved.

The architecture of the novel three-finger end effector architecture is illustrated in Fig. 3. The gripper comprises of a palm, an end part, three sliders, three fingers, six revolute joints, and six prismatic joints. The three fingers are arranged symmetrically, allowing for the symmetrical movement of the fingers. Taking one finger branch as an example, the finger is connected to the slider via a revolute joint, while the slider has a connection with the end part, forming the prismatic joint simultaneously. The linear movement of the finger is achieved by the prismatic joint between the finger and palm. The palm and end part are connected by a revolute joint, which permits the relative rotation between them. For the mechanism, the end part can output rotational motion, which is also the input motion for the gripper. Thus, the rotation of the end part can be utilized to control the opening and closing of the gripper.
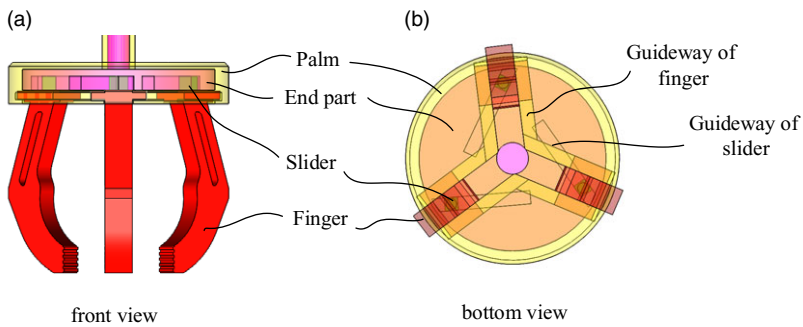
Figure 4 presents the kinematics of the gripper, where the joints and components are expressed in the same color as in the 3D model. The dotted line denotes the initial state in which configuration the angles between the lines LP and PQ and PQ and LQ are represented by γ_0 and γ_1, respectively. γ is the

Figure 1. *Two-limb gripper mechanism.*

Worm gear
transmission

Figure 2. *2-DOF driving system.*

(a)

(b)

Palm

End part

Slider

Finger

Guideway of
finger

Guideway of
slider

front view

bottom view
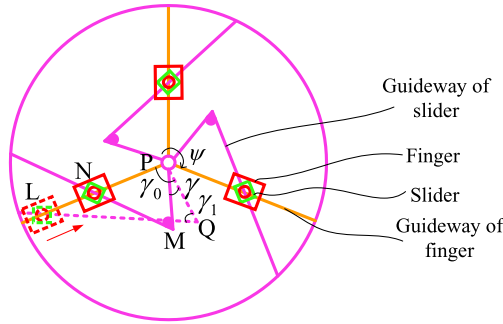
Figure 3. *Gripper architecture.*
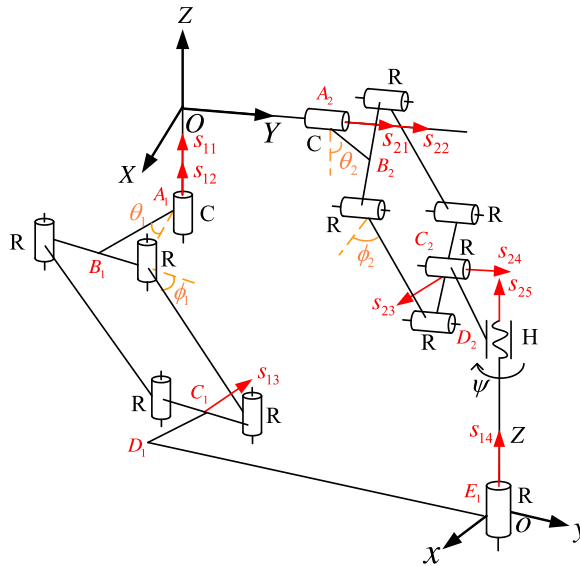
Figure 4. *Kinematics of the gripper.*

Figure 5. *Geometric scheme of the manipulator.*

rotational angle of the end part. During the design procedure, the angles γ_0 and γ_1 as well as the length of MP can be specified. According to the geometric relationship, the length of MN can be calculated by the following equation:

$$|MN| = \frac{|PQ| \sin(\gamma_0 - \gamma)}{\sin(\pi - \gamma_0 + \gamma + \gamma_1)} \tag{1}$$

Then, the length of NP can be obtained by:

$$|NP| = |MP| \cos(\gamma_0 - \gamma) + |MN| \cos(\pi - \gamma_0 + \gamma + \gamma_1) \tag{2}$$

Thus, the opening distance, that is, the length of LN, can be computed by:

$$|LN| = |LP| - |NP| \tag{3}$$

The geometric scheme of the two-limb mechanism is presented in Fig. 5. To facilitate the kinematic study, at the intersection point between the guide rails of the active prismatic joint A_1 and A_2, the origin O is established as the reference point for the global coordinate system. The Z-axis coincides with the direction of joint A_1, and the Y-axis is directed along the movement of joint A_2. The end effector is equipped with a moving coordinate system, aligned such that its x-, y-, and z-axes run parallel to the X-, Y-, and Z-axes of the fixed coordinate system, respectively. The angle θ_1 is measured from the dotted

line parallel to the X-axis to A_1B_1, while θ_2 is determined from the dotted line parallel to the Z-axis to A_2B_2. θ_1 and θ_2 denote the input angles. Additionally, the angle ϕ_1 is calculated from the dotted line parallel to the short rod to the long rod of parallelogram joint, while ϕ_2 is given by measuring from the dotted line parallel to the short rod to the long rod of parallelogram joint. The unit vectors collinear with the axes of different joints are labeled as s_{ij}. ψ is the rotational angle of the screw joint. It can be observed that the first kinematic chain lies in the XOY plane, whereas the second kinematic chain lies in the XOZ plane.

Based on screw theory [43], the properties of output motion can be explored. A generalized prismatic joint can replace the parallelogram joint, allowing movement along the direction perpendicular to the long rod. The branch motion-screw systems for two kinematic chains can be written as:

$$\{\$_1^m\} = \begin{cases} \$_{11} = \begin{bmatrix} 0 & 0 & 0; & 0 & 0 & 1 \end{bmatrix}^T \\[2mm] \$_{12} = \begin{bmatrix} 0 & 0 & 1; & 0 & 0 & 0 \end{bmatrix}^T \\[2mm] \$_{13} = \begin{bmatrix} 0 & 0 & 0; & -\dfrac{\cot(\phi_1+\theta_1)}{\sqrt{1+\cot^2(\phi_1+\theta_1)}} & \dfrac{1}{\sqrt{1+\cot^2(\phi_1+\theta_1)}} & 0 \end{bmatrix}^T \\[4mm] \$_{14} = \begin{bmatrix} 0 & 0 & 1; & y_{14} & -x_{14} & 0 \end{bmatrix}^T \end{cases} \tag{4}$$

$$\{\$_2^m\} = \begin{cases} \$_{21} = \begin{bmatrix} 0 & 0 & 0; & 0 & 1 & 0 \end{bmatrix}^T \\[2mm] \$_{22} = \begin{bmatrix} 0 & 1 & 0; & 0 & 0 & 0 \end{bmatrix}^T \\[2mm] \$_{23} = \begin{bmatrix} 0 & 0 & 0; & \dfrac{\cot(\phi_2+\theta_2)}{\sqrt{1+\cot^2(\phi_2+\theta_2)}} & 0 & \dfrac{1}{\sqrt{1+\cot^2(\phi_2+\theta_2)}} \end{bmatrix}^T \\[4mm] \$_{24} = \begin{bmatrix} 0 & 1 & 0; & -z_{24} & 0 & x_{24} \end{bmatrix}^T \\[2mm] \$_{25} = \begin{bmatrix} 0 & 0 & 1; & y_{25} & -x_{25} & p \end{bmatrix}^T \end{cases} \tag{5}$$

where $\{\$_i^m\}$ ($i = 1, 2$) is the motion-screw systems of two chains, $\$_{ij}$ ($i = 1, 2$ and $j = 1, 2, \ldots, 5$) denotes the motion screws of joints in the two chains, and $\begin{pmatrix} x_{ij} & y_{ij} & z_{ij} \end{pmatrix}^T$ represents the position of the jth joint in the ith limb, and p is the pitch of the helical joint. Then, the branch constraint-screws systems that are reciprocal to motion-screw systems can be obtained as:

$$\{\$_1^r\} = \begin{cases} \$_{11}^r = \begin{bmatrix} 0 & 0 & 0; & 1 & 0 & 0 \end{bmatrix}^T \\[2mm] \$_{12}^r = \begin{bmatrix} 0 & 0 & 0; & 0 & 1 & 0 \end{bmatrix}^T \end{cases} \tag{6}$$

$$\$_2^r = \begin{bmatrix} 0 & 0 & 0; & 1 & 0 & 0 \end{bmatrix}^T \tag{7}$$

Note that the reciprocal screws $\$_{11}^r$ and $\$_{12}^r$ indicate that the first kinematic chain exerts two couples parallel to the x- and y-axis on the moving platform, whereas $\$_2^r$ represents the couple parallel to the x-axis from the second kinematic chain. The constraint-screw systems provide two constraint couples on the platform, which limits the rotations around the x- and y-axis. A common constraint couple acting about x-axis is obtained. Hence, the number of common constraint is 1, that is, $\lambda = 1$. Also, no redundant constraint exists in this mechanism, that is, $v = 0$. According to its equivalent mechanism, the mechanism is comprised of nine basic components and nine lower joints. Thus, the number of DOF is computed by the modified Kutzbach–Grübler formula [44] as follows:

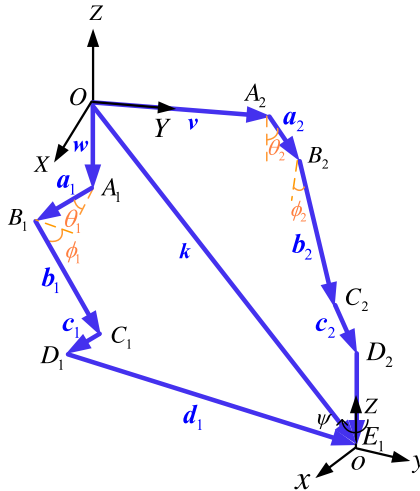$$M = d(n-g-1) + \sum_{i=1}^{g} f_i + v = 5(9-9-1) + 9 = 4 \tag{8}$$

Figure 6. *Vector notation for the kinematic modeling.*

where d is the order of the mechanism, $d = 6 - \lambda$, n denotes the number of basic components, g represents the number of joints, f_i indicates the DOF of ith joints, and v is the number of redundant constraints.

Based on the analysis, the mechanism is a Schönflies motion generator if the three-finger end effector is removed. The rotation around the z-axis here is utilized to control the opening and closing of the three-finger end effector. Therefore, the whole DOF of the gripper mechanism remains at 4, which include three translational motions and grasp operation. Due to the structural restrictions in the motion, the geometry relationship between the joints remains unchanged, resulting in a noninstantaneous DOF.

3. Kinematics

The mechanism after removing the three-finger end effector possesses three translations in space plus one rotation around a given axis. The pose variables of the end effector can be given by $\boldsymbol{x}[\begin{array}{cccc} x & y & z & \psi \end{array}]^\mathrm{T}$. The input variables of the four actuators are provided by $\boldsymbol{q}[\begin{array}{cccc} q_1 & q_2 & \theta_1 & \theta_2 \end{array}]^\mathrm{T}$. The vector notation for the kinematic modeling of its equivalent simplified mechanism is presented in Fig. 6. The length of links are defined as $A_iB_i = l_{i1}$, $B_iC_i = l_{i2}$, $C_iD_i = l_{i3}$, and $D_1E_1 = l_{14}$. The vector loop closure equations are utilized for both position and velocity analysis. Two equations can be obtained:

$$\begin{cases} q_1\boldsymbol{w} + l_{11}\boldsymbol{a}_1 + l_{12}\boldsymbol{b}_1 + l_{13}\boldsymbol{c}_1 + l_{14}\boldsymbol{d}_1 = \boldsymbol{k} \\ q_2\boldsymbol{v} + l_{21}\boldsymbol{a}_2 + l_{22}\boldsymbol{b}_2 + l_{23}\boldsymbol{c}_2 + p\psi\boldsymbol{w} = \boldsymbol{k} \end{cases} \tag{9}$$

where the vectors are defined as follows:

$$\boldsymbol{w} = [\begin{array}{ccc} 0 & 0 & -1 \end{array}]^\mathrm{T}, \boldsymbol{v} = [\begin{array}{ccc} 0 & 1 & 0 \end{array}]^\mathrm{T}, \boldsymbol{k} = [\begin{array}{ccc} x & y & z \end{array}]^\mathrm{T}, \boldsymbol{a}_1 = \boldsymbol{c}_1 = [\begin{array}{ccc} \cos\theta_1 & -\sin\theta_1 & 0 \end{array}]^\mathrm{T},$$

$$\boldsymbol{b}_1 = [\begin{array}{ccc} \sin(\phi_1 + \theta_1) & \cos(\phi_1 + \theta_1) & 0 \end{array}]^\mathrm{T}, \boldsymbol{d}_1 = [\begin{array}{ccc} \sin\theta_1 & \cos\theta_1 & 0 \end{array}]^\mathrm{T}, \boldsymbol{a}_2 = [\begin{array}{ccc} \sin\theta_2 & 0 & \cos\theta_2 \end{array}]^\mathrm{T},$$

$$\boldsymbol{b}_2 = [\begin{array}{ccc} \cos(\phi_2 - \theta_2) & 0 & \sin(\phi_2 - \theta_2) \end{array}]^\mathrm{T}, \boldsymbol{c}_2 = [\begin{array}{ccc} 1 & 0 & 0 \end{array}]^\mathrm{T}.$$

Further, Eq. (9) can be simplified as:

$$\begin{cases} l_{11}\cos\theta_1 + l_{12}\sin(\phi_1 + \theta_1) + l_{13}\cos\theta_1 + l_{14}\sin\theta_1 = x \\ -l_{11}\sin\theta_1 + l_{12}\cos(\phi_1 + \theta_1) - l_{13}\sin\theta_1 + l_{14}\cos\theta_1 = y \\ -q_1 = z \end{cases} \tag{10}$$

$$\begin{cases} l_{21} \sin \theta_2 + l_{22} \cos (\phi_2 - \theta_2) + l_{23} = x \\ q_2 = y \\ l_{21} \cos \theta_2 + l_{22} \sin (\phi_2 - \theta_2) - p\psi = z \end{cases} \tag{11}$$

Based on the results presented in Eqs. (10) and (11), it can be concluded that the output translation along the z-axis is a function of the input variable q_1, while the output translation along the y-axis is dependent on the input variable q_2. These equations demonstrate that the proposed manipulator exhibits partial decoupling of input–output motions, which facilitates precise control and enhances accuracy.

3.1. Inverse kinematic problems

For inverse kinematic problems, the positon of the end effector $\boldsymbol{x}[\begin{matrix} x & y & z & \psi \end{matrix}]^{\mathrm{T}}$ is given, and the input variables $\boldsymbol{q}[\begin{matrix} q_1 & q_2 & \theta_1 & \theta_2 \end{matrix}]^{\mathrm{T}}$ need to be computed.

Squaring both sides of the first two equations in Eq. (10) yields

$$g_1 = g_2 \cos \theta_1 - g_3 \sin \theta_1 \tag{12}$$

where $g_1 = l_{11}^2 + l_{13}^2 + l_{14}^2 + 2l_{11}l_{13} + x^2 + y^2 - l_{12}^2$, $g_2 = 2(l_{11}x + l_{13}x + l_{14}y)$, $g_3 = 2(-l_{14}x + l_{11}y + l_{13}y)$.

Hence, the input variable θ_1 can be derived as:

$$\theta_1 = 2 \arctan \left(\frac{-g_3 \pm \sqrt{-g_1^2 + g_2^2 + g_3^2}}{g_1 + g_2} \right) \tag{13}$$

Similarly, by squaring both sides of the first and the last equations in Eq. (11), an equation is obtained:

$$s_1 = s_2 \cos \theta_2 - s_3 \sin \theta_2 \tag{14}$$

where $s_1 = l_{21}^2 + l_{23}^2 + x^2 + z^2 + (p\psi)^2 - l_{22}^2 + 2pz\psi - 2l_{23}x$, $s_2 = 2l_{21}(p\psi + z)$, $s_3 = 2l_{21}(l_{23} - x)$.

Then, the input variable θ_2 is computed:

$$\theta_2 = 2 \arctan \left(\frac{s_3 \pm \sqrt{-s_1^2 + s_2^2 + s_3^2}}{s_1 + s_2} \right) \tag{15}$$

Since the two inputs of two prismatic joints can be obtained directly due to partial decoupling motion, the input parameters can be found as follows:

$$\begin{cases} q_1 = -z \\ q_2 = y \\ \theta_1 = f_1 (x, y) \\ \theta_2 = f_2 (x, z, \psi) \end{cases} \tag{16}$$

3.2. Direct kinematic problems

For direct kinematic problems, the input parameters $\boldsymbol{q}[\begin{matrix} q_1 & q_2 & \theta_1 & \theta_2 \end{matrix}]^{\mathrm{T}}$ are known, and the aim is to determine the coordinates of the end effector $\boldsymbol{x}[\begin{matrix} x & y & z & \psi \end{matrix}]^{\mathrm{T}}$.

Squaring both sides of the first two equations in Eq. (10) yields

$$m_1 = -x^2 + m_2 x \tag{17}$$

where $m_1 = l_{11}^2 + l_{13}^2 + 2l_{11}l_{13} + l_{14}^2 + y^2 - l_{12}^2 - 2l_{14}y \cos \theta_1 + 2(l_{11} + l_{13})y \sin \theta_1$, $m_2 = 2[(l_{11} + l_{13}) \cos \theta_1 + l_{14} \sin \theta_1]$.

Consequently, the position along the x-coordinate can be derived as:

$$x = \frac{1}{2} \left(m_2 \pm \sqrt{-4m_1 + m_2^2} \right) \tag{18}$$

Squaring both sides of the first and the last equations in Eq. (11) yields

$$n_1 p\psi + (p\psi)^2 = n_2 \tag{19}$$

where $n_1 = 2z - 2l_{21}\cos\theta_2$, $n_2 = l_{22}^2 + 2l_{23}x - l_{21}^2 - l_{23}^2 - x^2 - z^2 - 2l_{21}(l_{23} - x)\sin\theta_2 + 2l_{21}z\cos\theta_2$.

Thus, the output rotation angle is calculated by:

$$\psi = \frac{\pm n_1 + \sqrt{n_1^2 + 4n_2}}{2p} \tag{20}$$

In summary, based on the above analysis, the position coordinates and the orientation of the end effector can be obtained as:

$$\begin{cases} x = F_1\,(q_2, \theta_1) \\ y = q_2 \\ z = -q_1 \\ \psi = F_2\,(q_1, q_2, \theta_1, \theta_2) \end{cases} \tag{21}$$

3.3. Velocity analysis

Based on the forgoing kinematic analysis, differentiation on both sides of Eq. (16) with respect of time yields

$$\boldsymbol{K}_x \dot{x} = \boldsymbol{K}_q \dot{q} \tag{22}$$

The Jacobian $\boldsymbol{J}$ can be obtained by:

$$\boldsymbol{J} = \boldsymbol{K}_q^{-1} \boldsymbol{K}_x \tag{23}$$

where

$$\dot{x} = [\dot{x} \quad \dot{y} \quad \dot{z} \quad \dot{\psi}]^T, \dot{q} = [\dot{\theta}_1 \quad \dot{\theta}_2 \quad \dot{q}_1 \quad \dot{q}_2]^T, \boldsymbol{K}_x = \begin{bmatrix} a_{11} & a_{12} & 0 & 0 \\ a_{21} & 0 & a_{23} & a_{24} \\ 0 & 1 & 0 & 0 \\ 0 & 0 & -1 & 0 \end{bmatrix},$$

$$\boldsymbol{K}_q = \begin{bmatrix} b_{11} & 0 & 0 & 0 \\ 0 & b_{22} & 0 & 0 \\ 0 & 0 & 1 & 0 \\ 0 & 0 & 0 & 1 \end{bmatrix}$$

with

$a_{11} = 2x - 2\cos\theta_1(l_{11} + l_{13}) - 2\sin\theta_1 l_{14}$, $a_{12} = 2y - 2\cos\theta_1 l_{14} + 2\sin\theta_1(l_{11} + l_{13})$,

$a_{21} = -2x + 2l_{23} + 2l_{21}\cos\theta_2$, $a_{23} = 2p\psi - 2z - 2l_{21}\sin\theta_2$, $a_{24} = 2pz + 2pl_{21}\sin\theta_2 - 2p\psi$,

$b_{11} = 2((l_{11} + l_{13})y - l_{14}x)\cos\theta_1 + 2((l_{11} + l_{13})x + l_{14}y)\sin\theta_1$,

$b_{22} = 2p\psi l_{21}\cos\theta_2 + 2l_{21}(l_{23} - x)\sin\theta_2 - 2l_{21}z\cos\theta_2$

Thus, the velocity equation of the proposed manipulator can be obtained as:

$$\boldsymbol{J}\dot{x} = \dot{q} \tag{24}$$

4. Performance evaluation of the gripper mechanism

Evaluating performance is an essential aspect of mechanical design. Some kinematic metrics are used to evaluate manipulator performance, such as singularity, workspace, manipulability, and dexterity. By analyzing these indices, designers can synthesize and construct manipulators that exhibit improved performance for practical applications. The Jacobian matrix and its properties, such as the determinant,
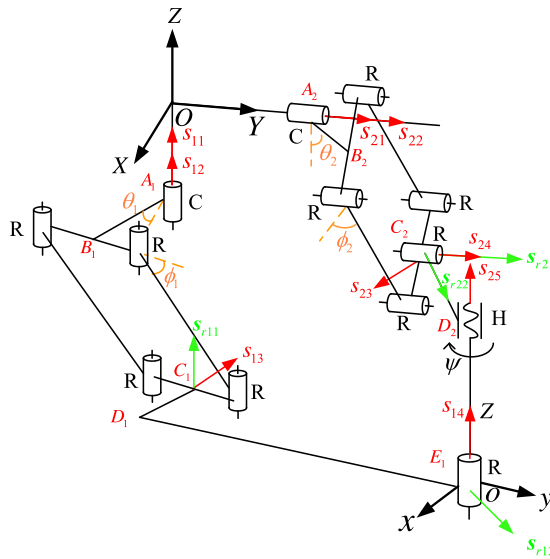
Figure 7. *Screws in the mechanism.*

eigenvalues, and condition number, serve as the basis for evaluating performance indices, making it an indispensable tool for analyzing the motion. Thus, the Jacobian matrix should be derived first.

4.1. Jacobian and singularity analysis

The Jacobian matrix plays a critical role in analyzing the singular configurations of a parallel manipulator by connecting the end effector velocity with the joint velocity. In this study, screw theory-based method [45] is used to solve the Jacobian matrix.

Singular configurations within the workspace of a parallel mechanism can limit its performance, as these configurations may cause a change in DOF of the mechanism, allowing the end effector to move even though all actuators are locked. This is undesirable in practical applications, and it can affect manipulability and control accuracy. Therefore, a manipulator should not only avoid singular configurations but also maintain a safe distance from the region close to singularity to ensure better kinematic performance and control. When the manipulator approaches a singular configuration, the relationship between the input motion and output motion distorts, leading to difficulty in control. Thus, singularity analysis is important for better kinematic performance and control of a manipulator.

The screws associated with the joints in the mechanism are presented in Fig. 7. The instantaneous twist of the end effector can be given as $\$_p = [\,w^T \quad v^T\,]^T$, where $w = [\,0 \quad 0 \quad w_z\,]^T$ and $v = [\,v_x \quad v_y \quad v_z\,]^T$ are referred to the angular velocity and linear velocity of the end effector, respectively. The detailed expression can be obtained by using the linear combination of all joints in each limb:

$$\$_P = \dot{q}_1\$_{11} + \dot{\theta}_1\$_{12} + w_{13}\$_{13} + \dot{\psi}\$_{24} \tag{25}$$

$$\$_P = \dot{q}_2\$_{21} + \dot{\theta}_2\$_{22} + w_{23}\$_{23} + w_{24}\$_{24} + \dot{\psi}\$_{25} \tag{26}$$

in which $\$_{ij}$ indicates the unit screw associated with the jth joint in the ith limb, $\dot{q}_i$ is the linear velocity of the actuated prismatic joints, while $\dot{\theta}_i$, w_{ij} and $\dot{\psi}$ denote the angular velocity of the actuated revolute joints, passive revolute joints, and screw joint, respectively.

The screws can be given as:

$$\$_{i1} = \begin{bmatrix} 0^{\mathrm{T}} & s_{i1}^{\mathrm{T}} \end{bmatrix}^{\mathrm{T}}$$

$$\$_{i2} = \begin{bmatrix} s_{i2}^{\mathrm{T}} & oA_i^{\mathrm{T}} \times s_{i2}^{\mathrm{T}} \end{bmatrix}^{\mathrm{T}}$$

$$\$_{i3} = \begin{bmatrix} 0^{\mathrm{T}} & s_{i3}^{\mathrm{T}} \end{bmatrix}^{\mathrm{T}}$$

$$\$_{14} = \begin{bmatrix} s_{14}^{\mathrm{T}} & 0 \end{bmatrix}^{\mathrm{T}}$$

$$\$_{24} = \begin{bmatrix} s_{24}^{\mathrm{T}} & oC_2^{\mathrm{T}} \times s_{24}^{\mathrm{T}} \end{bmatrix}^{\mathrm{T}} \tag{27}$$

in which $s_{11} = s_{12} = s_{14} = \begin{bmatrix} 0 & 0 & 1 \end{bmatrix}^{\mathrm{T}}$, $s_{21} = s_{22} = s_{24} = \begin{bmatrix} 0 & 1 & 0 \end{bmatrix}^{\mathrm{T}}$,

$$s_{13} = \begin{bmatrix} -\dfrac{\cot(\phi_1 + \theta_1)}{\sqrt{1 + \cot^2(\phi_1 + \theta_1)}} & \dfrac{1}{\sqrt{1 + \cot^2(\phi_1 + \theta_1)}} & 0 \end{bmatrix}^{\mathrm{T}},$$

$$s_{23} = \begin{bmatrix} \dfrac{\cot(\phi_2 + \theta_2)}{\sqrt{1 + \cot^2(\phi_2 + \theta_2)}} & 0 & \dfrac{1}{\sqrt{1 + \cot^2(\phi_2 + \theta_2)}} \end{bmatrix}^{\mathrm{T}}.$$

To eliminate certain passive joint screws, we use the theory of reciprocal screws. Specifically, when locking the actuated prismatic in the first limb, a screw denoted as $\$_{r11}$ can be identified that is reciprocal to all screws but $\$_{11}$. This screw is parallel to the axes of $\$_{12}$ and $\$_{14}$ and simultaneously perpendicular to the axis of $\$_{13}$:

$$\$_{r11} = \begin{bmatrix} s_{r11}^{\mathrm{T}} oC_1^{\mathrm{T}} \times s_{r11}^{\mathrm{T}} \end{bmatrix}^{\mathrm{T}} \tag{28}$$

After locking the actuated revolute joint in the first limb, a screw can be found as $\$_{r12}$ that is reciprocal to all screws besides $\$_{12}$. This screw intersects with $\$_{14}$ and is parallel to the normal direction of the plane determined by the vectors s_{11} and s_{13}:

$$\$_{r12} = \begin{bmatrix} s_{r12}^{\mathrm{T}} 0 \end{bmatrix}^{\mathrm{T}} \tag{29}$$

Taking the orthogonal products of both sides of Eq. (25) with (28) and (29) in turn yields

$$\$_{r11}^{\mathrm{T}} \$_P = \dot{q}_1 \$_{r11}^{\mathrm{T}} \$_{11} \tag{30}$$

$$\$_{r12}^{\mathrm{T}} \$_P = \dot{\theta}_1 \$_{r12}^{\mathrm{T}} \$_{12} \tag{31}$$

When locking the actuated prismatic joint in the second limb, a screw denoted as $\$_{r21}$ can be identified that is reciprocal to all screws apart from $\$_{21}$. This screw is parallel to the axes of $\$_{22}$ and $\$_{24}$ and simultaneously perpendicular to $\$_{23}$:

$$\$_{r21} = \begin{bmatrix} s_{r21}^{\mathrm{T}} oC_2^{\mathrm{T}} \times s_{r21}^{\mathrm{T}} \end{bmatrix}^{\mathrm{T}} \tag{32}$$

After locking the actuated revolute joint in the second limb, a screw can be found as $\$_{r22}$ that is reciprocal to all screws but $\$_{22}$. This screw intersects with $\$_{24}$ and $\$_{25}$ simultaneously and is parallel to the normal direction of the plane determined by the vectors s_{21} and s_{23}:

$$\$_{r22} = \begin{bmatrix} s_{r22}^{\mathrm{T}} oC_2^{\mathrm{T}} \times s_{r22}^{\mathrm{T}} \end{bmatrix}^{\mathrm{T}} \tag{33}$$

Taking the orthogonal products of both sides of Eq. (26) with (32) and (33) in turn yields

$$\$_{r21}^{\mathrm{T}} \$_P = \dot{q}_2 \$_{r21}^{\mathrm{T}} \$_{21} \tag{34}$$

$$\$_{r22}^{\mathrm{T}} \$_P = \dot{\theta}_2 \$_{r22}^{\mathrm{T}} \$_{22} \tag{35}$$

Based on the above analysis, Eqs. (30), (31), (34), and (35) can be rewritten in matrix form:

$$
\begin{bmatrix} \$_{r11}^{\mathrm{T}} \\ \$_{r12}^{\mathrm{T}} \\ \$_{r21}^{\mathrm{T}} \\ \$_{r22}^{\mathrm{T}} \end{bmatrix} \$_P = \begin{bmatrix} \$_{r11}^{\mathrm{T}}\$_{11} & & & \\ & \$_{r12}^{\mathrm{T}}\$_{12} & & \\ & & \$_{r21}^{\mathrm{T}}\$_{21} & \\ & & & \$_{r22}^{\mathrm{T}}\$_{22} \end{bmatrix} \begin{bmatrix} \dot{q}_1 \\ \dot{\theta}_1 \\ \dot{q}_2 \\ \dot{\theta}_2 \end{bmatrix} \tag{36}
$$

Equation (36) can also be expressed in a general form as:

$$
\boldsymbol{J}_x \$_P = \boldsymbol{J}_q \dot{q} \tag{37}
$$

where $\boldsymbol{J}_x = \begin{bmatrix} \$_{r11}^{\mathrm{T}} \\ \$_{r12}^{\mathrm{T}} \\ \$_{r21}^{\mathrm{T}} \\ \$_{r22}^{\mathrm{T}} \end{bmatrix}, \boldsymbol{J}_q = \begin{bmatrix} \$_{r11}^{\mathrm{T}}\$_{11} & 0 & 0 & 0 \\ 0 & \$_{r12}^{\mathrm{T}}\$_{12} & 0 & 0 \\ 0 & 0 & \$_{r21}^{\mathrm{T}}\$_{21} & 0 \\ 0 & 0 & 0 & \$_{r22}^{\mathrm{T}}\$_{22} \end{bmatrix}, \dot{q} = \begin{bmatrix} \dot{q}_1 \\ \dot{\theta}_1 \\ \dot{q}_2 \\ \dot{\theta}_2 \end{bmatrix}$

By analyzing the obtained Jacobian matrix, it is possible to identify singular configurations.

4.1.1. Inverse kinematic singularity
If any of the diagonal elements of the matrix $\boldsymbol{J}_q$ are zero, it can lead to the occurrence of the inverse kinematic singularity in the mechanism. After performing calculations, the equation $\$_{r11}^{\mathrm{T}}\$_{11} = \$_{r21}^{\mathrm{T}}\$_{21} = 1$ can be obtained. Therefore, the inverse kinematic singularity occurs when $\$_{r12}^{\mathrm{T}}\$_{12} = 0$ or $\$_{r22}^{\mathrm{T}}\$_{22} = 0$. Then the following relations can be obtained:

$$
\$_{r12}^{\mathrm{T}}\$_{12} = s_{12}^{\mathrm{T}} \left(\boldsymbol{oA}_1^{\mathrm{T}} \times s_{r12}^{\mathrm{T}} \right) \tag{38}
$$

$$
\$_{r22}^{\mathrm{T}}\$_{22} = s_{22}^{\mathrm{T}} \left(s_{r22}^{\mathrm{T}} \times \boldsymbol{C}_2\boldsymbol{A}_2^{\mathrm{T}} \right) \tag{39}
$$

If these three vectors s_{12}, $\boldsymbol{oA}_1$, and s_{r12} are coplanar, which means that the projection of oA_1 and $\mathrm{B}_1\mathrm{C}_1$ on the *XOY* plane are parallel to each other, and the mechanism moves to the singular configuration. This is the case illustrated in Fig. 8(a). When the three vectors s_{22}, $\boldsymbol{C}_2\boldsymbol{A}_2$, and s_{r22} are coplanar, that is, the long rod and the short rod in the parallelogram joint form a right angle, Eq. (39) is equal to zero. The singular configuration is depicted in Fig. 8(b).
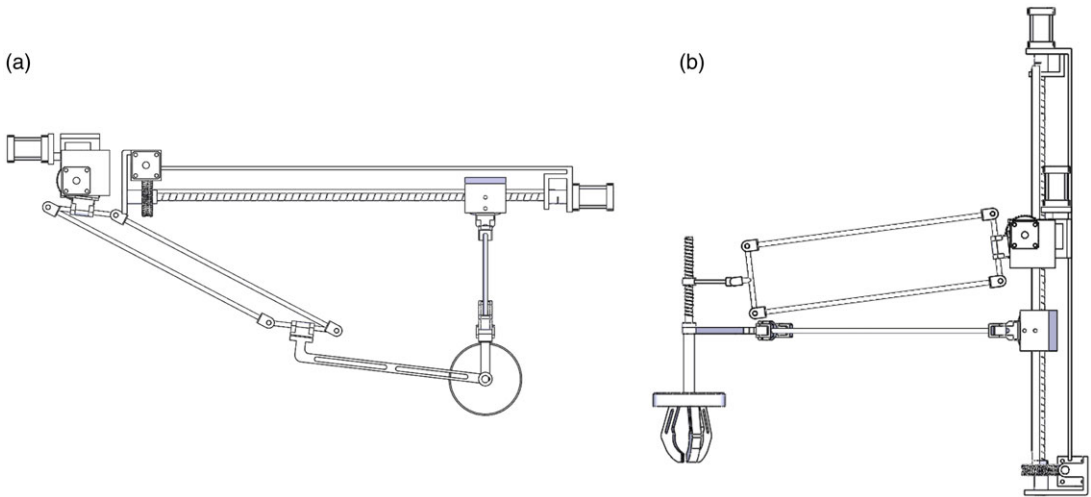
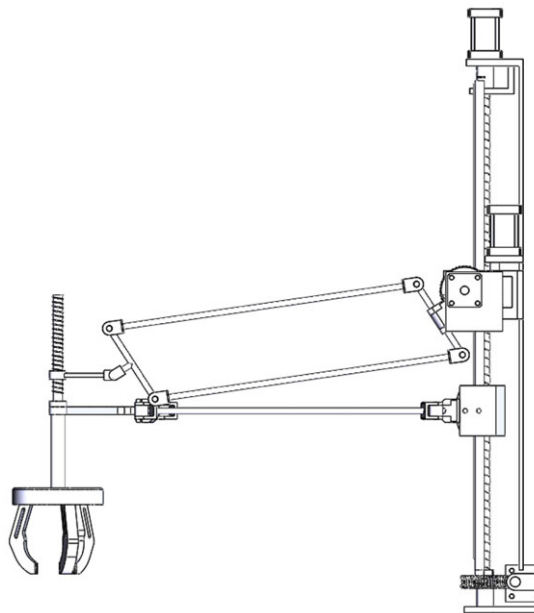### 4.1.2. Forward kinematic singularity
From Eq. (37), we can obtain

$$
\boldsymbol{J}_x = \begin{bmatrix} s_{r11}^{\mathrm{T}} & \boldsymbol{oC}_1^{\mathrm{T}} \times s_{r11}^{\mathrm{T}} \\ s_{r12}^{\mathrm{T}} & 0 \\ s_{r21}^{\mathrm{T}} & \boldsymbol{oC}_2^{\mathrm{T}} \times s_{r21}^{\mathrm{T}} \\ s_{r22}^{\mathrm{T}} & \boldsymbol{oC}_2^{\mathrm{T}} \times s_{r22}^{\mathrm{T}} \end{bmatrix} \tag{40}
$$

When the matrix $\boldsymbol{J}_x$ is rank-deficient, the forward kinematic singularity occurs. There is a zero element in this matrix. If there are two or more zero elements in the matrix, the matrix is rank-deficient. First, when $\boldsymbol{oC}_1^{\mathrm{T}} \times s_{r11}^{\mathrm{T}}$ is equal to zero, the vectors $\boldsymbol{oC}_1$ and s_{r11} coincide with each other. According to the structural limitations, this case does not exist. Second, when $\boldsymbol{oC}_2^{\mathrm{T}} \times s_{r21}^{\mathrm{T}}$ is equal to zero, the vector $\boldsymbol{oC}_2$ should coincide with s_{r21}. Similarly, due to the structural limitations, this case does not exist, either. Finally, $\boldsymbol{oC}_2^{\mathrm{T}} \times s_{r22}^{\mathrm{T}}$ vanishes, which means that the vector $\boldsymbol{oC}_2$ coincides with s_{r22}. This is the case illustrated in Fig. 9.

Furthermore, the inverse and forward kinematic singular surfaces in the joint space and workspace are presented in Figs. 10 and 11 utilizing the structural parameters that were previously introduced.

Figure 8. *Inverse kinematic singular configurations: (a) case 1 and (b) case 2.*

Figure 9. *Forward kinematic singular configuration.*

4.2. Workspace analysis

The workspace of a manipulator is a critical evaluation metric used to assess the ability of the moving platform to achieve different poses, which significantly influences the manipulator's performance. One common limitation of parallel mechanisms is their limited workspace. Generally, among manipulators with the same DOF, a larger workspace is preferable. In this section, the reachable workspace is analyzed. The primary factors that influence the manipulator's workspace include the length limit of links, the angle limit of rotational joints, and interference issues between different links and the moving platform. It is essential to analyze the reachable workspace to optimize the manipulator's design and ensure that it can achieve the desired performance.
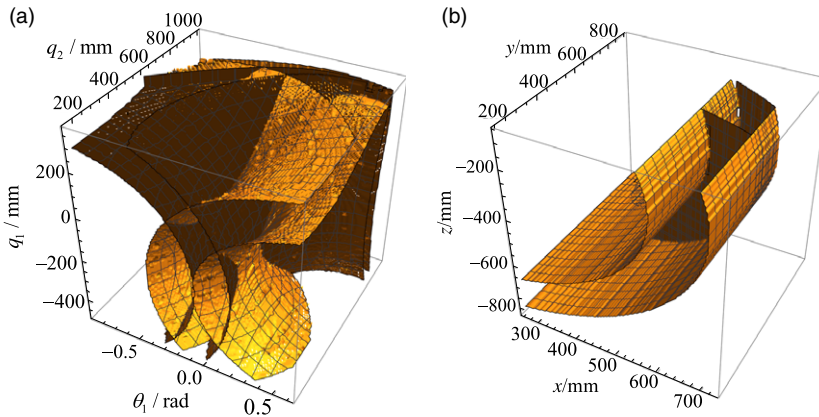
Figure 10. *Inverse kinematic singular surfaces: (a) in the joint space and (b) in the workspace.*
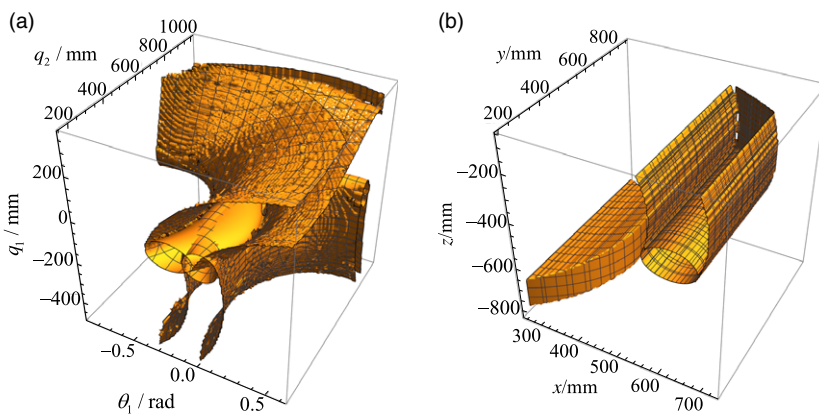

Figure 11. *Forward kinematic singular surfaces: (a) in the joint space and (b) in the workspace.*

The stroke of the first and second active prismatic joints are set to $-500\,\text{mm} \leq q_1 \leq 350\,\text{mm}$ and $150\,\text{mm} \leq q_2 \leq 1000\,\text{mm}$, respectively, and the rotational angles of the first and second active rotational joints are in the range of $-50\,\text{deg} \leq \theta_1 \leq 35\,\text{deg}$ and $-35\,\text{deg} \leq \theta_2 \leq 50\,\text{deg}$, respectively.

According to the structural characteristics, the rotational angles ϕ_1 and ϕ_2 are calculated in detail to avoid the interference between links:

$$\phi_1 = \arccos\left(\boldsymbol{b}_1\boldsymbol{c}_1 \cdot \boldsymbol{v}\right) \tag{41}$$

$$\phi_2 = \arccos\left(\boldsymbol{b}_2\boldsymbol{c}_2 \cdot \boldsymbol{u}\right) \tag{42}$$

in which $\boldsymbol{b}_1\boldsymbol{c}_1$ and $\boldsymbol{b}_2\boldsymbol{c}_2$ are normalized vectors of vectors $\boldsymbol{B}_1\boldsymbol{C}_1$ and $\boldsymbol{B}_2\boldsymbol{C}_2$, respectively, and $\boldsymbol{u}$ and $\boldsymbol{v}$ are unit vectors along the X- and Y-axis, respectively. The expressions for these vectors can be given by:

$$\boldsymbol{b}_1\boldsymbol{c}_1 = \frac{\boldsymbol{B}_1\boldsymbol{C}_1}{|\boldsymbol{B}_1\boldsymbol{C}_1|}, \boldsymbol{b}_2\boldsymbol{c}_2 = \frac{\boldsymbol{B}_2\boldsymbol{C}_2}{|\boldsymbol{B}_2\boldsymbol{C}_2|}, \boldsymbol{u} = \begin{bmatrix} 1 & 0 & 0 \end{bmatrix}^{\mathrm{T}}, \boldsymbol{v} = \begin{bmatrix} 0 & 1 & 0 \end{bmatrix}^{\mathrm{T}} \tag{43}$$

Therefore, the rotational angle ϕ_1 between the long rod of the parallelogram joint and the Y-axis should be limited to $45\,\text{deg} \leq \phi_1 \leq 100\,\text{deg}$, and ϕ_2 between the long rod of the parallelogram joint and the X-axis should be in the range of $-25\,\text{deg} \leq \phi_2 \leq 70\,\text{deg}$.

For a parallel manipulator, the reachable workspace comprises the set of points that can be reached by the end effector. Hence, based on the structure parameters in Table I, the inverse kinematic solution

Table I.* *Structural parameters.

Parameters	l_{11}	l_{12}	l_{13}	l_{14}	l_{21}	l_{22}	l_{23}	p
Value (mm)	65	550	60	400	65	550	90	8
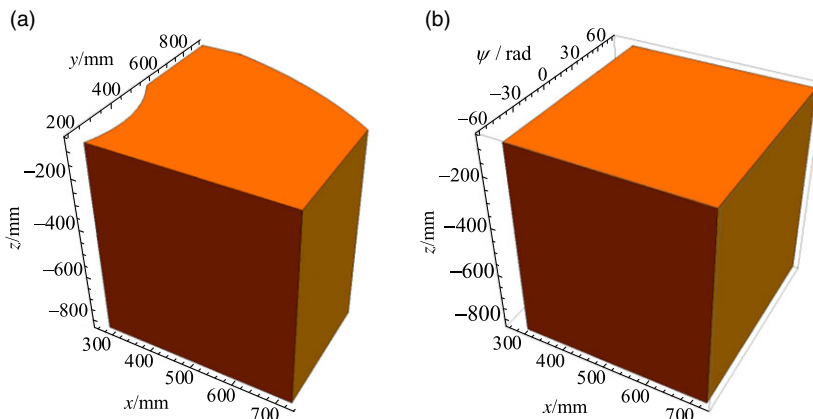
**Figure 12.** *Workspace: (a) in the space (x y z) and (b) in the space (x ψ z).*

is employed to calculate the reachable workspace. Then, according to the limitations of $q_1, q_2, \theta_1, \theta_2, \phi_1$ and ϕ_2 obtained above, the points meeting these constraints can be selected. The reachable workspaces of the proposed mechanism are studied in the space (x y z) with the orientation $\psi = 0$ and the space (x ψ z) with the coordinate $y = 400$ mm, respectively. The workspaces are depicted in Fig. 12 using Mathematica software. According to the kinematic analysis, the y- and z-coordinate are related to the input variables q_2 and q_1, respectively. As shown in Fig. 12(a), the 3D workspace can be interpreted as extruding the *xoy* plane along the *z*-axis, effectively illustrating the characteristic decoupling motion in the *z* direction. The kinematic solution indicates that the mechanism also possesses the characteristic of decoupling motion in the *y* direction. However, we acknowledge that Fig. 12(a) reveals a coupling relationship between the displacement in the *x* direction and the displacement in the *y* direction. This coupling is a consequence of the interaction between the actuated parameter q_2 and the position along the *x*-coordinate.

Additionally, Figs. 10(b) and 11(b) plot all kinematic solutions leading to singular configurations within the manipulator's workspace. The relationship between the reachable workspace and the inverse kinematic singularity inside the reachable workspace is proposed in Fig. 13(a), while the relationship between the reachable workspace and the forward singularity inside the reachable workspace is depicted in Fig. 13(b). The green surface in both figures represents the singular surface within the reachable workspace. To enhance the manipulator's performance, avoiding singular loci is crucial. In future work, the avoidance of singular loci will be investigated by planning the manipulator's trajectory to expand its workspace.
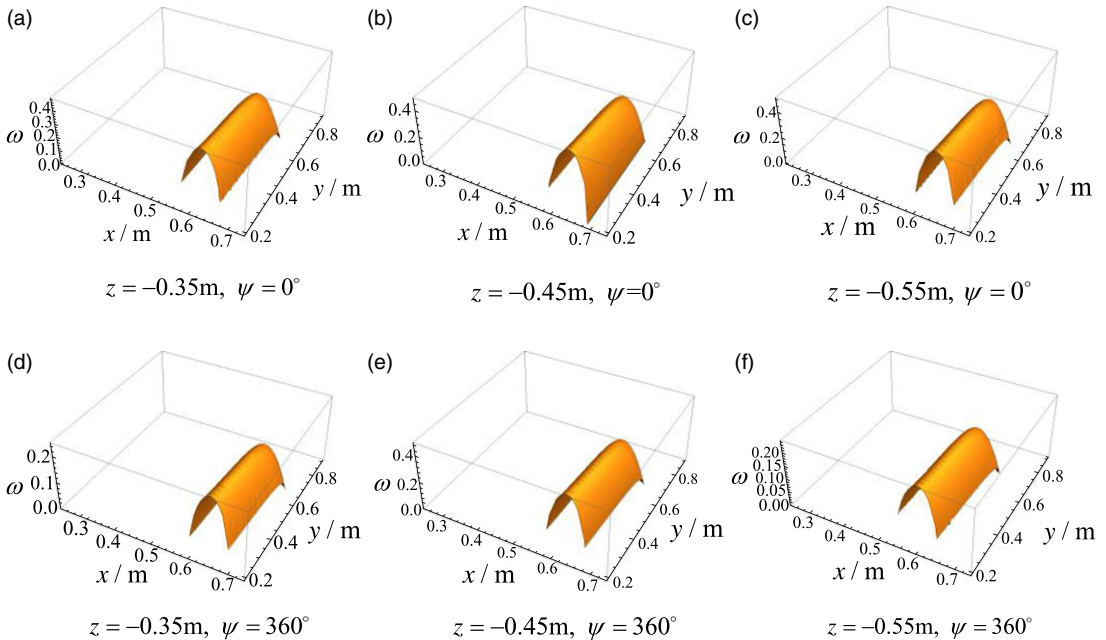
4.3. Manipulability

The kinematic manipulability index is used to evaluate the capability of velocity transmission of a manipulator and can also be considered as an equivalent measure of the dexterity [46]. According to the definition in [47], the kinematic manipulability is the square root of the determinant of JJ^{T}. The detailed expression can be given by:

$$\omega = \sqrt{\det\left(JJ^{\mathrm{T}}\right)} \tag{44}$$
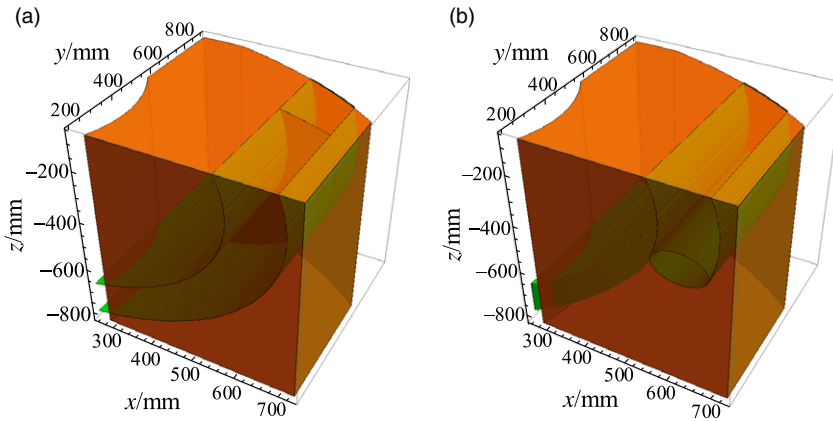
Figure 13. *Inverse kinematic singular surface (a) and forward kinematic singular surface (b) within the reachable workspace.*

Figure 14. *Kinematic manipulability for various z-value and rotational angles within the workspace.*

It should be noted that the Jacobian matrix is posture-dependent, and as a result, the kinematic manipulability is a local performance index. However, it provides a clear indication of whether the manipulator is in a singular configuration. When the value of ω is close to or equal to 0, the manipulator is in or near a singular configuration. Hence, the value of ω is desired to be greater than 0 to avoid the singular configurations.

Based on the structure parameters, the kinematic manipulability for various z-value and rotational angles within the workspace can be calculated. The results are presented in Fig. 14. As can be observed, the value of kinematic manipulability is close to 0 when the end effector moves to the boundary along the x-axis or y-axis.

4.4. Dexterity analysis

The dexterity of a manipulator is a critical measure of its kinematic performance in pick-and-place applications, defined as the ability to move to any position or direction and apply forces or torques in any direction [48]. The condition number of the Jacobian matrix is used to evaluate the dexterity of a manipulator [49,50], with a lower value indicating better dexterity. In particular, the inverse of the condition number, which ranges from 0 to 1, is commonly used as a measure. Some studies [51–55] have also used dexterity to evaluate the accuracy and sensitivity of a manipulator. Specifically, a higher dexterity tends to lead to higher accuracy. Although manipulability is a related concept, dexterity is a more appropriate measure for evaluating accuracy in many cases.

The kinetostatic conditioning index (KCI) is a posture-independent index. As defined in [56], the expression can be given by:

$$\text{KCI} = \frac{1}{\kappa_{\min}} \times 100\% \tag{45}$$

where $\kappa_{\min}$ is the minimum condition number. When $\kappa_{\min}$ is equal to 1, the KCI is 100%. Then, the manipulator has the istropic characteristics, which means that the manipulator possesses good motion transmission performance.

In order to evaluate the dexterity within the whole workspace, the global conditioning index (GCI) is proposed [49]. The expression can be given by:

$$\text{GCI} = \frac{\int_W \frac{1}{\kappa} dV}{V} \tag{46}$$

in which W is the whole workspace and V is the volume of the workspace.

However, different types of degrees of freedom (i.e., three translational motions and one rotation) presents the challenge for unifying the units of each element in the Jacobian matrix and representing the physical meaning of the manipulator with the condition number. To solve this problem, Altuzarra [57] proposed a method to normalize the nonhomogeneous Jacobian matrix using the concept of characteristic length. The detailed expression of the homogeneous Jacobian matrix $\boldsymbol{J}_h$ can be defined as:

$$\boldsymbol{J}_{\text{h}} = \begin{pmatrix} \boldsymbol{A} & \frac{1}{L}\boldsymbol{B} \end{pmatrix} \tag{47}$$

where L is the characteristic length, $\boldsymbol{A}$ represents the 4×3 submatrix formed by the first three columns of $\boldsymbol{J}$, and $\boldsymbol{B}$ denotes the 4×1 submatrix formed by the fourth column of $\boldsymbol{J}$.

After normalizing the nonhomogeneous Jacobian matrix, the Jacobian matrix $\boldsymbol{J}_{\text{h}}$ can attain dimensionally homogeneous. The isotropy condition can be given by:

$$\boldsymbol{J}_{\text{h}}^{\text{T}}\boldsymbol{J}_{\text{h}} = \begin{bmatrix} \boldsymbol{A}^{\text{T}}\boldsymbol{A} & \frac{1}{L}\boldsymbol{A}^{\text{T}}\boldsymbol{B} \\ \frac{1}{L}\boldsymbol{B}^{\text{T}}\boldsymbol{A} & \frac{1}{L^2}\boldsymbol{B}^{\text{T}}\boldsymbol{B} \end{bmatrix} = \sigma^2\boldsymbol{I} \tag{48}$$

where σ is a nondimensional scalar and $\boldsymbol{I}$ denotes the 4×4 identity matrix. The manipulator is considered isotropic when the homogeneous Jacobian matrix becomes isotropic. If there is no solution to the isotropy condition, then the manipulator is nonisotropic.

From Eq. (48), we can obtain the following relationships:

$$\text{tr}\left(\boldsymbol{A}^{\text{T}}\boldsymbol{A}\right) = 3\sigma^2 \tag{49}$$

$$\frac{1}{L}\boldsymbol{A}^{\text{T}}\boldsymbol{B} = \boldsymbol{0} \tag{50}$$

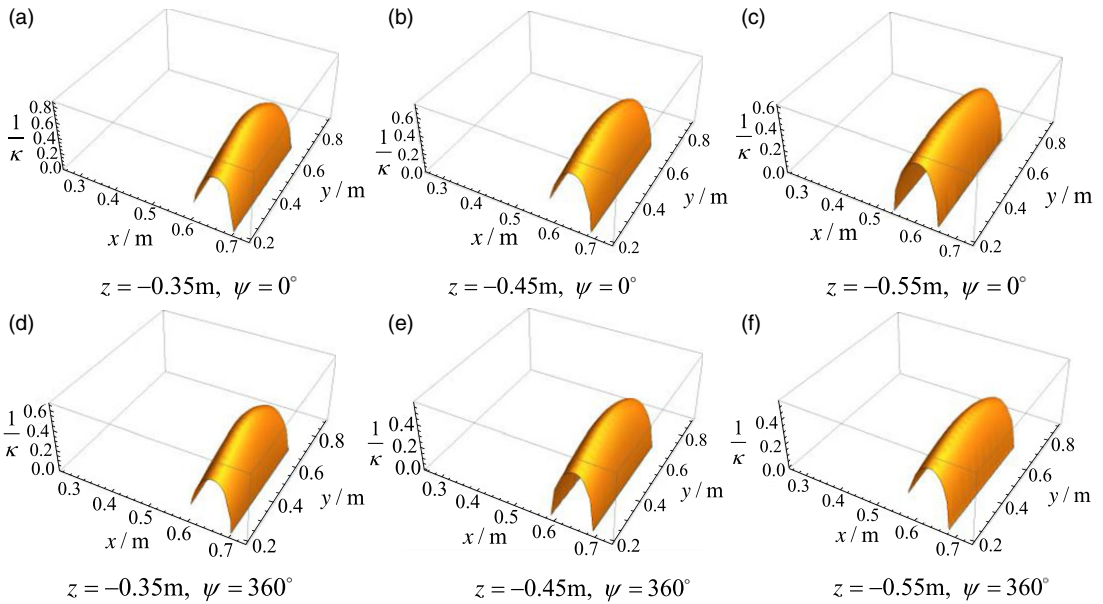$$\frac{1}{L^2}\boldsymbol{B}^{\text{T}}\boldsymbol{B} = \sigma^2 \tag{51}$$

Figure 15. *Reciprocal of Jacobian matrix condition number.*

Then, the characteristic length can be expressed as:

$$L = \sqrt{\frac{3\boldsymbol{B}^{\mathrm{T}}\boldsymbol{B}}{\mathrm{tr}\left(\boldsymbol{A}^{\mathrm{T}}\boldsymbol{A}\right)}} \tag{52}$$

The condition number κ of the homogeneous Jacobian matrix $\boldsymbol{J}_{\mathrm{h}}$ can be calculated by:

$$\kappa = \|\boldsymbol{J}_{\mathrm{h}}\| \, \|\boldsymbol{J}_{\mathrm{h}}^{-1}\| \tag{53}$$

in which $\|\cdot\|$ indicates the norm of the matrix argument. It should be noted that Frobenius norm is frame-invariant and analytic. Hence, the calculation of the condition number by means of the Frobenius norm can be expressed as:

$$\kappa = \frac{1}{4}\sqrt{\mathrm{tr}\left(\boldsymbol{J}_{\mathrm{h}}^{\mathrm{T}}\boldsymbol{J}_{\mathrm{h}}\right)\mathrm{tr}\left[\left(\boldsymbol{J}_{\mathrm{h}}^{\mathrm{T}}\boldsymbol{J}_{\mathrm{h}}\right)^{-1}\right]} \tag{54}$$

Based on the structure parameters, the value of the characteristic length can be calculated as $L = 0.2171$ m. The KCI is depicted in Fig. 15 with various z-values and rotational angles. According to the analytical results, the maximum KCI over the whole workspace is observed when the end effector is located at $x = 0.65$ m and $y = 0.5$ m, indicating that the manipulator has better performance in this position. Additionally, smaller values of KCI correspond to smaller z-coordinate magnitudes and larger rotational angles. Conversely, the value of KCI approaches zero at the boundary of the workspace, suggesting that the manipulator is less dexterous in these postures, and this region should be avoided.

However, to the best of our knowledge, the Jacobian matrix is configuration-dependent. The local conditioning number varies with different postures and provides a local indication of dexterity of a manipulator. To obtain a global measure of dexterity within the entire workspace, the GCI is calculated. The expression in Eq. (46) is too complicated to compute the value of GCI. Furthermore, the value of $1/\kappa$ can be zero in some postures, indicating that singularity occurs in these postures. Hence, a simplified numerical approach in ref. [48] is used to approximate the GCI value:

$$\mathrm{GCI} = \frac{1}{N}\sum_{i}^{N}\frac{1}{\kappa_i} \tag{55}$$

where the workspace is discretized into a set of N points and κ_i is the value of κ at the ith point. Therefore, the results can be calculated by researching the points within the workspace. The larger the value of GCI, the higher the global dexterity. The GCI of the proposed manipulator can be obtained as GCI = 0.2754.

5. Parameter optimization

In the previous section, the dexterity of the proposed manipulator was studied and corresponding charts were plotted. The optimization of the manipulator parameters was carried out to improve its dexterity in this section, which is an essential factor in the design of manipulators. The analytical results of the dexterity of the proposed manipulator can be used to guide the optimization of the parameters. From the perspective of practical applications, the length of links is not determined arbitrarily. The objective of the optimization was to find the appropriate length of links that result in improved dexterity. To achieve this objective, the parameter-finiteness normalization method proposed by Liu [58] was used. This method reduces the number of parameters from n to $(n-1)$ and defines logical bounds for each parameter. The parameters optimization procedure makes it possible to reveal the relationship between the dexterity and the parameters in a limited space. The process of design optimization can be described as follows:

Step 1. Identification of design parameters. According to the geometric relationship in the structure, let $l_{11} = l_{21}, l_{12} = l_{22}, l_{13} = 1.2l_{11}, l_{23} = 2l_{21}$. Then, the three design parameters can be determined as l_{11}, l_{12}, and l_{14}.

Step 2. Determination of parameter design space (PDS). According to the definition in [58], the normalization factor of the manipulator is obtained by:

$$D = \frac{l_{11} + l_{12} + l_{14}}{3} \tag{56}$$

The three nondimensional parameters can be calculated by:

$$r_1 = \frac{l_{11}}{D}, r_2 = \frac{l_{12}}{D}, r_3 = \frac{l_{14}}{D} \tag{57}$$

For this proposed manipulator, the normalized parameters should be specified as:

$$\begin{cases} r_1 + r_2 + r_3 = 3 \\ r_2 \succ r_1 \\ r_3 \succ r_1 \end{cases} \tag{58}$$
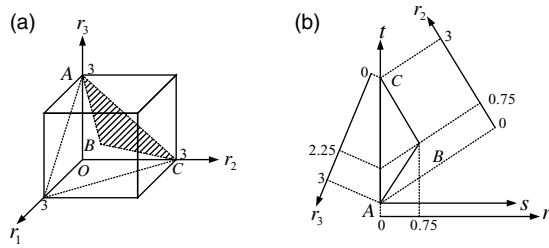
Then, the PDS for the proposed manipulator defined by Eq. (58) is depicted as the shaded triangle ABC in Fig. 16(a), where all possible design parameters values are included. Figure 16(b) shows the triangle ABC in a plan view. In the plan space, the design parameters can be expressed as:

$$\begin{cases} r_1 = s \\ r_2 = \frac{\sqrt{3}}{3}t - \frac{1}{2}s \\ r_3 = 3 - \frac{\sqrt{3}}{3}t - \frac{1}{2}s \end{cases} \tag{59}$$
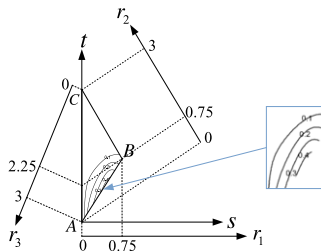
or

$$\begin{cases} s = r_1 \\ t = \frac{\sqrt{3}(3 + r_2 - r_3)}{2} \end{cases} \tag{60}$$

Step 3. We identify the optimum region. Herein, let D = 400. For each set of values (s, t), there is a set of corresponding values of design parameters (r_1, r_2, r_3). Using the design parameters, the GCI is

Figure 16. *Parameter design space of the proposed manipulator: (a) spatial space and (b) plan view.*

Figure 17. *Distribution of GCI in the parameter design space.*

calculated. The relationship between the dexterity and the normalized parameters in the PDS is illustrated in Fig. 17. It is noteworthy that the optimum region is the intersection between the dexterity chart and the PDS. Therefore, the proposed manipulator can be studied in this finite optimal design region.

Step 4. We select a candidate from the optimal region. The optimum region in Fig. 17 contains all possible normalized parameters for different optimal manipulators. As can be seen in Fig. 17, the GCI has a large value in the region $s \in [0.4, 0.5]$ and $t \in [1.0, 1.1]$. Thus, 10 groups of candidates are chosen whose GCI is larger than 0.4. The values of design parameters, optimized length, and GCI are listed in Table II.

Step 5. Check whether the optimized parameters meet the design objectives. If the optimized parameters can meet the design objective, then the optimal design is finished; otherwise, we return to Step 4.

Table II shows that the first 10 group data are chosen from the optimal region, whose GCI is larger than 0.4. The last group parameters are measured from the model of the proposed manipulator in Fig. 1. The objective of the optimization is to find the appropriate length of links, where the proposed manipulator has a better dexterity. The proposed manipulator with No. 10 optimal parameters will have better dexterity.

6. Conclusion

This paper presents a novel two-limb gripper mechanism with an integrated three-finger end effector. The mechanism is composed of only a small number of lower pairs and components, which simplifies manufacturing and installation. The simple two-limb structure also avoids interference between the limbs and platform, providing a fairly large workspace. To address the issue of moving actuators, the mechanism employs a 2-DOF driving system. The gripper mechanism possesses a decoupled motion property that makes it easy to control and plan its trajectory. To enhance its industrial application, we evaluate the performance of the proposed manipulator and optimize its parameters for improved dexterity.

In future work, we plan to analyze the stiffness and dynamic properties of the gripper mechanism. Additionally, we will carry out trajectory planning to avoid singular loci and optimize the workspace.

Table II. *Optimized parameters and corresponding GCI.*

No.	s	t	r_1	r_2	r_3	l_{11}	l_{12}	l_{13}	l_{14}	l_{21}	l_{22}	l_{23}	GCI
1	0.42	1.05	0.42	0.61	1.97	168.00	242.49	201.60	789.51	168.00	242.49	336.00	0.4201
2	0.42	1.08	0.42	0.62	1.96	168.00	249.42	201.60	782.59	168.00	249.42	336.00	0.4089
3	0.44	1.02	0.44	0.59	1.97	176.00	235.56	211.20	788.44	176.00	235.56	352.00	0.4566
4	0.44	1.05	0.44	0.61	1.95	176.00	242.49	211.20	781.51	176.00	242.49	352.00	0.4450
5	0.46	1.07	0.46	0.62	1.92	184.00	247.11	220.80	768.89	184.00	247.11	368.00	0.4601
6	0.46	1.09	0.46	0.63	1.91	184.00	251.73	220.80	764.28	184.00	251.73	368.00	0.4520
7	0.48	1.04	0.48	0.60	1.92	192.00	240.18	230.40	767.82	192.00	240.18	384.00	0.4921
8	0.48	1.06	0.48	0.61	1.91	192.00	244.80	230.40	763.20	192.00	244.80	384.00	0.4838
9	0.50	1.03	0.50	0.59	1.91	200.00	237.87	240.00	762.13	200.00	237.87	400.00	0.4891
10	0.50	1.07	0.50	0.62	1.88	200.00	247.11	240.00	752.89	200.00	247.11	400.00	0.4951
11	0.16	2.38	0.16	1.37	1.46	65.00	550.00	60.00	400.00	65.00	550.00	90.00	0.2754

To validate its performance, a prototype will be fabricated. These advancements will improve the efficiency and reliability of the gripper mechanism, making it a valuable addition to the field of robotics.

References

[1] J. P. Merlet, *Parallel Robots (Solid Mechanics and Its Applications)* (Springer, Dordrecht, 2006).

[2] L. W. Tsai, *Robot Analysis: The Mechanics of Serial and Parallel Manipulators* (John Wiley & Sons, New York, 1999).

[3] Z. Huang, F. F. Xi, T. Huang, J. S. Dai and R. Sinatra, "Lower-mobility parallel robots: Theory and applications," *Adv. Mech. Eng.* **2**, 927930 (2010). doi: 10.1155/2010/927930.

[4] Q. C. Li, L. M. Xu, Q. H. Chen and W. Ye, "New family of RPR-equivalent parallel mechanisms: Design and application," *Chin. J. Mech. Eng.* **30**(2), 217–221 (2017).

[5] S. Krut, O. Company, V. Nabat and F. Pierrot, "Heli4: A Parallel Robot for Scara Motions with a Very Compact Traveling Plate and a Symmetrical Design," **In:** *Proceedings of the 2006 IEEE/RSJ International Conference on Intelligent Robots and Systems, China* (2006) pp. 1656–1661.

[6] L. Rolland, "The Manta and the Kanuk: Novel 4 Dof Parallel Mechanism for Industrial Handling," **In:** *Proceeding of ASME Dynamic Systems and Control Division IMECE'99 Conference, USA*, vol. **67** (1999) pp. 831–844.

[7] Y. K. Tu, Q. H. Chen, W. Ye and Q. C. Li, "Kinematics singularity, and optimal design of a novel 3T1R parallel manipulator with full rotational capability," *J. Mech. Sci. Technol.* **32**(6), 2877–2887 (2018).

[8] R. Clavel, "A Fast Robot with Parallel Geometry," **In:** *International Symposium on Industrial Robots* (1988) pp. 91–100.

[9] F. Pierrot and O. Company, "H4: A New Family of 4-DOF Parallel Robots," **In:** *IEEE/ASME International Conference on Advanced Intelligent Mechatronics, USA* (1999) pp. 508–513.

[10] S. Krut, M. Benoit, H. Ota and F. Pierrot, "I4: A New Parallel Mechanism for Scara Motions," **In:** *IEEE International Conference on Robotics and Automation, Taiwan* (2003) pp. 1875–1880.

[11] V. Nabat, M. de la O Rodriguez, O. Company, S. Krut and F. Pierrot, "Par4: Very High Speed Parallel Robot for Pick-and-Place," **In:** *IEEE/RSJ International Conference on Intelligent Robots and Systems, Canada* (2005) pp. 55–558.

[12] F. G. Xie and X. J. Liu, "Analysis of the kinematic characteristics of a high-speed parallel robot with Schönflies motion: Mobility, kinematics, and singularity," *Front. Mech. Eng.* **11**(2), 135–143 (2016).

[13] O. Salgado, O. Altuzrra, V. Petuya and A. Hernandez, "Synthesis and design of a novel 3T1R fully-parallel manipulator," *J. Mech. Des.* **130**(4), 042305 (2008).

[14] C. X. Tian, Y. F. Fang and Q. J. Ge, "Design and analysis of a partial decoupled generalized parallel mechanism for 3T1R motion," *Mech. Mach. Theory* **140**, 211–232 (2019). doi: 10.1016/j.mechmachtheory.2019.06.001.

[15] J. Zhao, C. C. Wu, G. L. Yang, C. Y. Chen, S. L. Chen, C. Y. Xiong and C. Zhang, "Kinematics analysis and workspace optimization for a 4-DOF 3T1R parallel manipulator," *Mech. Mach. Theory* **167**, 104484 (2022).

[16] J. Gallardo-Alvarado, R. Rodriguez-Castro and P. J. Delissantos-Lara, "Kinematics and dynamics of a 4-PRUR Schönflies parallel manipulator by means of screw theory and the principle of virtual work," *Mech. Mach. Theory* **122**, 347–360 (2018). doi: 10.1016/j.mechmachtheory.2021.104484.

[17] S. Guo, Y. Wei, H. B. Qu, D. Zhang and Y. F. Fang, "A serial of novel four degrees of freedom parallel mechanisms with large rotational workspace," *Robotica* **34**(4), 764–776 (2016).

[18] S. Guo, Y. F. Fang and H. B. Qu, "Type synthesis of 4-DOF nonoverconstrained parallel mechanisms based on screw theory," *Robotica* **30**(1), 31–37 (2012).

[19] X. Zhang, M. X. Yang, D. J. Mu and H. R. Wang, "Unified formulas of constrained Jacobian and Hessian matrices for 3T1R overconstrained parallel mechanisms," *Mech. Based Des. Struct. Mach.* **51**(3), 1431–1445 (2023).

[20] P. Rossi, R. Simoni, H. Simas and A. P. Carboni, "Kinematic Analysis of a 3T1R Fully Decoupled Parallel Manipulators Family," **In:** *Multibody Mechatronic Systems. MuSMe 2021. Mechanisms and Machine Science*, vol. **94** (2021) pp. 102–109.

[21] X. W. Kong and C. M. Gosselin, "Type synthesis of 3T1R 4-DOF parallel manipulators based on screw theory," *IEEE Trans. Robot. Autom.* **20**(2), 181–190 (2004).

[22] R. D. Gregorio, "A Novel Single-Loop Decoupled Schoenflies-Motion Generator: Concept and Kinematics Analysis," **In:** *Advances in Service and Industrial Robotics. RAAD 2017. Mechanisms and Machine Science*, vol. **49** (2017) pp. 11–18.

[23] H. Simas and R. D. Gregorio, "Kinetostatics and Optimal Design of a 2PRPU Schoenflies-Motion Generator," **In:** *Multibody Mechatronic Systems* (2017) pp. 141–150.

[24] O. Company, F. Pierrot, V. Nabat and M. de la O Rodriguez, "Schoen Flies Motion Generator: A New Non Redundant Parallel Manipulator with Unlimited Rotation Capability," **In:** *Proceedings of the IEEE International Conference on Robotics and Automation* (2005) pp. 3250–3255.

[25] C. Lee and J. M. Hervé, "Isoconstrained parallel generators of Schoenflies motion," *J. Mech. Robot.* **3**(2), 021006 (2011).

[26] Shadow Robot Company, "Design of a Dextrous Hand for Advanced CLAWAR Applications," **In:** *Proceedings of the 6th International Conference on Climbing and Walking Robots and the Supporting Technologies for Mobile Machine* (2003) pp. 691–698.

[27] M. Grebenstein, A. Albu-Schffer, T. Bahls, M. Chalon, O. Eiberger, W. Friedl, R. Gruber, S. Haddadin, U. Hagn, R. Haslinger, H. Höppner, S. Jörg, M. Nickl, A. Nothhelfer, F. Petit, J. Reill, N. Seitz, T. Wimböck, S. Wolf, T. Wüsthoff and G. Hirzinger, "The DLR Hand Arm System," **In:** *2011 IEEE International Conference on Robotics and Automation* (2011) pp. 3175–3182.

[28] P. Vulliez, J. Gazeau, P. Laguillaumie, H. Mnyusiwalla and P. Seguin, "Focus on the mechatronics design of a new dexterous robotic hand for inside hand manipulation," *Robotica* **36**(8), 1206–1224 (2018).

[29] R. Deimel and O. Brock, "A novel type of compliant and underactuated robotic hand for dexterous grasping," *Int. J. Robot. Res.* **35**(1-3), 161–185 (2016).

[30] H. Wang, F. J. Abu-Dakka, T. Nguyen Le, V. Kyrki and H. Xu, "A novel soft robotic hand design with human-inspired soft palm," *IEEE Robot. Autom. Mag.* **28**(2), 37–49 (2021).

[31] A. Lotfiani, H. Zhao, Z. Shao and X. Yi, "Torsional stiffness improvement of a soft pneumatic finger using embedded skeleton," *J. Mech. Robot.* **12**(1), 1–23 (2019).

[32] S. Abondance, C. B. Teeplea and R. J. Wood, "A dexterous soft robotic hand for delicate in-hand manipulation," *IEEE Robot. Autom. Lett.* **5**(4), 5502–5509 (2020).

[33] W. Hu and G. Alici, "Bioinspired three-dimensional-printed helical soft pneumatic actuators and their characterization," *Soft Robot.* **7**(3), 267–282 (2020).

[34] C. B. Teeple, T. N. Koutros, M. A. Graule and R. J. Wood, "Multisegment soft robotic fingers enable robust precision grasping," *Int. J. Robot. Res.* **39**(14), 1647–1667 (2020).

[35] S. Yao, M. Ceccarelli, G. Carbone and Z. Dong, "Grasp configuration planning for a low-cost and easy-operation underactuated three-fingered robot hand," *Mech Mach. Theory* **129**, 51–69 (2018). doi: 10.1016/j.mechmachtheory.2018.06.019.

[36] S. Hasegawa, K. Wada, Y. Niitani, K. Okada and M. Inaba, "A Three-Fingered Hand with a Suction Gripping System for Picking Various Objects in Cluttered Narrow Space," **In:** *Proceedings of the 2017 IEEE/RSJ International Conference on Intelligent Robots and Systems* (2017) pp. 1164–1171.

[37] M. Maggi, G. Mantriota and G. Reina, "Influence of the dynamic effects and grasping location on the performance of an adaptive vacuum gripper," *Actuators* **11**(2), 55 (2022).

[38] P. Bryan, S. Kumar and F. Sahin, "Design of a Soft Robotic Gripper for Improved Grasping with Suction Cups," **In:** *Proceedings of the 2019 IEEE International Conference on Systems, Man and Cybernetics (SMC)* (2019) pp. 2405–2410.

[39] X. Jin, Y. Fang, D. Zhang and J. Gong, "Design of dexterous hands based on parallel finger structures," *Mech. Mach. Theory* **152**, 103952 (2020). doi: 10.1016/j.mechmachtheory.2020.103952.

[40] C. X. Tian and D. Zhang, "Design and analysis of novel kinematically redundant reconfigurable generalized parallel manipulators," *Mech. Mach. Theory* **166**, 104481 (2021). doi: 10.1016/j.mechmachtheory.2021.104481.

[41] L. Wang, Y. F. Fang and L. Q. Li, "Design and analysis of the gripper mechanism based on generalized parallel mechanisms with configurable moving platform," *Front. Mech. Eng.* **16**(4), 765–781 (2021).

[42] L. Wang, Y. Fang, D. Zhang and L. Li, "Design and analysis of partially decoupled translational parallel mechanisms with single-loop structures," *Front. Mech. Eng.* **17**(3), 39 (2022).

[43] Y. F. Fang and L. W. Tsai, "Enumeration of a class of overconstrained mechanisms using the theory of reciprocal screws," *Mech. Mach. Theory* **39**(11), 1175–1187 (2004).

[44] Z. Huang and Q. C. Li, "Type synthesis of symmetrical lower-mobility parallel mechanisms using constraint-synthesis method," *Int. J. Robot. Res.* **22**(1), 59–79 (2003).

[45] L. W. Tsai, *Robot Analysis: The Mechanics of Serial and Parallel Manipulators* (John Wiley & Sons, New York, 1999).

[46] J. P. Merlet, "Jacobian, manipulability, condition number, and accuracy of parallel robots," *J. Mech. Des.* **128**(1), 199–206 (2006).

[47] T. Yoshikawa, "Manipulability of robotic mechanisms," *Int. J. Robot. Res.* **4**(2), 3–9 (1985).

[48] Y. M. Li and Q. S. Xu, "Kinematic analysis of a 3-PRS parallel manipulator," *Robot. Comput. Integr. Manuf.* **23**(4), 395–408 (2007).

[49] C. Gosselin and J. Angeles, "A global performance index for the kinematic optimization of robotic manipulators," *J. Mech. Des.* **113**(3), 220–226 (1991).

[50] J. P. Merlet, "Jacobian, manipulability, condition number, and accuracy of parallel robots," *J. Mech. Des.* **128**(1), 199–206 (2006).

[51] M. Tannous, S. Caro and A. Goldsztejn, "Sensitivity analysis of parallel manipulators using an interval linearization method," *Mech. Mach. Theory* **71**, 93–114 (2014). doi: 10.1016/j.mechmachtheory.2013.09.004.

[52] G. Pond and J. A. Carretero, "Formulating Jacobian matrices for the dexterity analysis of parallel manipulators," *Mech. Mach. Theory* **41**(12), 1505–1519 (2006).

[53] A. Yu, I. Bonev and P. Zsombor-Murray, "Geometric approach to the accuracy analysis of a class of 3-DOF planar parallel robots," *Mech. Mach. Theory* **43**(3), 364–375 (2009).

[54] H. S. Kim and L. W. Tsai, "Design optimization of a Cartesian parallel manipulator," *J. Mech. Des.* **125**(1), 43–51 (2003).

[55] S. Briot and I. A. Bonev, "Accuracy analysis of 3-DOF planar parallel robots," *Mech. Mach. Theory* **43**(4), 445–458 (2007).

[56] J. Angeles, *Fundamentals of Robotic Mechanical Systems Theory, Methods, and Algorithms* (Springer, Cham, 2014).

[57] O. Altuzarra, A. Hernandez, O. Salgado and J. Angeles, "Multiobjective optimum design of a symmetric parallel Schönflies-motion generator," *J. Mech. Des.* **131**(3), 031002 (2009).

[58] X. J. Liu and J. S. Wang, "A new methodology for optimal kinematic design of parallel mechanisms," *Mech. Mach. Theory* **42**(9), 1210–1224 (2007).